Small Animal Radionuclide Imaging With Focusing Gamma-Ray Optics

MJ Pivovaroff, WB Barber, FE Christensen, WW Craig, T Decker, M Epstein, T Funk, CJ Hailey, BH Hasegawa, R Hill, JG Jernigan, C Taylor, K Ziock

1 March 2004

Small animal radionuclide imaging
with focusing gamma-ray optics

M. J. Pivovaroff[a,b], W. B. Barber[c], F. E. Christensen[d], W. W. Craig[b], T. Decker[b],
M. Epstein[b,e], T. Funk[c], C. J. Hailey[f], B. H. Hasegawa[c,g],
R. Hill[b], J. G. Jernigan[a], C. Taylor[f], K. Ziock[b]

[a]University of California, Berkeley, Space Sciences Laboratory; Berkeley CA, USA
[b]Lawrence Livermore National Laboratory; Livermore CA, USA
[c]University of California, San Francisco, Department of Radiology; San Francisco CA, USA
[d]Danish Space Research Institute, Space Sciences Laboratory; Copenhagen, Denmark
[e]California Institute of Technology, Department of Engineering; Pasadena CA, USA
[f]Columbia University; New York NY, USA
[g]University of California, Berkeley and University of California, San Francisco, Joint
Bioengineering Graduate Group; Berkeley CA USA

ABSTRACT

Significant effort currently is being devoted to the development of noninvasive imaging systems that allow *in vivo* assessment of biological and biomolecular interactions in mice and other small animals. While physiological function in small animals can be localized and imaged using conventional radionuclide imaging techniques such as single-photon emission tomography (SPECT) and positron emission tomography (PET), these techniques inherently are limited to spatial resolutions of $1-2$ mm. For this reason, we are developing a small animal radionuclide imaging system (SARIS) using grazing incidence optics to focus gamma-rays emitted by ^{125}I and other radiopharmaceuticals. We have developed a prototype optic with sufficient accuracy and precision to focus the 27.5 keV photons from ^{125}I onto a high-resolution imaging detector. Experimental measurements from the prototype have demonstrated that the optic can focus X-rays from a microfocus X-ray tube to a spot having physical dimensions (approximately 1500 microns half-power diameter) consistent with those predicted by theory. Our theoretical and numerical analysis also indicate that an optic can be designed and build that ultimately can achieve 100 μm spatial resolution with sufficient efficiency to perform *in vivo* single photon emission imaging studies in small animal.

Keywords: SPECT, small animal imaging, gamma-ray optics, X-ray optics

1. INTRODUCTION

1.1. Biological Motivation for Small Animal Imaging

Animal models, especially transgenic and knock-out mice, now affect research in every area of biomedical science and are available for a diverse range of human conditions.[1] In the neurosciences,[2] transgenic animals have contributed greatly to shed light on basic mechanisms of brain function, behavior,[3] and human neurological disorders.[4] By creating and analyzing animals that harbor precise, preplanned changes in candidate genes, researchers in pharmacology[4,5] are rapidly making progress toward uncovering how drugs exert their effects, including the mechanisms of action of alcohol and anesthetics.[6] The role of transgenic and knockout mice in cancer research is profound and widespread. These studies are providing insight into the complex events contributing to the induction of DNA damage, repair, mutagenesis, and carcinogenesis.[7] The availability of transgenic animals facilitates the development of therapeutic techniques, including the use of drugs and antibodies[8,9] and the understanding of molecular control elements which govern normal and abnormal cell and organ function.[5,10] Similarly, advances in transgenic approaches have produced genetically engineered mice

---

Send correspondence to M. Pivovaroff, E-mail: pivovaroff1@llnl.gov

with unique cardiovascular phenotypes, and with which researchers can investigate mammalian cardiovascular development, differentiation, function, and disease.[11, 12]

It is clear from these examples that transgenic animal technology now has an essential role and profound influence in all areas of biomedical research. For these reasons, several investigators have developed high-resolution techniques suitable for noninvasive imaging of small animals. Anatomical studies can be performed using high resolution magnetic resonance imaging or high-resolution CT,[13–16] whereas magnetic resonance spectroscopy[12, 17, 18] can be used to assay the regional concentrations of metabolites. Although these techniques provide spatial resolution in the range $R = 25 - 50$ μm, noninvasive metabolic and functional assessments are best performed using radionuclide imaging techniques such as positron emission tomography (PET) and single-photon emission computed tomography (SPECT). Several investigators[19–23] are developing dedicated PET systems with sufficient spatial resolution (1 to 2 mm) for metabolic studies with ^{18}F-fluorodeoxyglucose, and to assess pharmacological events[24] in small animals. Radionuclide imaging techniques for single-photon agents also are needed since these agents are relatively inexpensive, widely available, and can be easily handled and are in common use in the laboratory setting. In addition, single photon labels such as ^{125}I and ^{111}In have longer half-lives needed for investigating uptake and biodistribution of labeled antibodies and other agents, while pharmaceuticals labelled with ^{99m}Tc are available for many functional measurements. Unfortunately, microscopic assessments of radiotracer distribution in mice currently can be measured only by tissue-sampling or autoradiography[25–27] after sacrificing the animal. Furthermore, these invasive techniques are labor intensive, and do not allow serial studies to be performed in the same animal. Therefore, single-photon radionuclide imaging techniques provide an important research tool for investigations with small animals,[28–30] especially critical for studies where noninvasive functional assessments are needed.

1.2. The need for sub-millimeter imaging

Ideally, one would like to have a technique that could image radionuclide distributions non-invasively at resolution comparable to MRI or CT modalities. Dramatically improving the spatial resolution is a pressing need for the community, as a variety of research problems can only be addressed with resolution on order of 100 μm. The impact these imaging capabilities will have in advancing all biomedical fields is easily seen by considering the specific areas of cardiovascular and cancer research.

There is a large body of work devoted to producing and refining mouse models of ischemic heart disease through the use of genetic engineering. Although these models provide excellent opportunities to study the progression of ischemic heart disease, the current imaging modalities cannot provide enough spatial resolution to utilize the murine models effectively. Current measures of myocardial function that occur on the sub-millimeter scale include progression of coronary artery disease, spatial correlation of sympathetic innervation and ischemia in congestive heart failure,[31] and angiogenesis and stem-cell localization being investigated for myocardial therapies.[32]

Carcinogenesis is thought to be initiated by only a few cells, perhaps only by a single malignant transformation. However, it is impossible to visualize such a small lesion with the current methods available to nuclear medicine. After all, a single cell measures just tens of microns, while a small group of cells may measure 100 μm in diameter. Waiting for a tumor to reach the 1 mm size accessible with conventional imaging techniques prevents study of the critical first stages of tumor development and prevention. Once identified, the small tumor can be monitored, it's response to therapeutics evaluated, and metastatic processes can be identified. Equally important, it is imperative to monitor the response of normal tissue or heterogeneous malignant foci adjacent to the lesion when therapeutics are applied. For example, small organs such as endocrine glands, cannot afford a millimeter uncertainty during tissue toxicity trials.

1.3. Current Approach for Radionuclide Imaging

Current imaging methods for single-photon radionuclide studies rely on absorptive collimation, with either a converging parallel hole collimator or a pinhole collimator serving as the optical element. Unfortunately, this approach has an inherent limitation between the achievable spatial resolution and efficiency of the system: the smaller the pinhole, the better the resolution, the lower the efficiency; or conversely, the larger the pinhole, the higher the efficiency, the poorer the resolution. Below, we derive the quantitative relationship between resolution

and efficiency for the case of a pinhole collimator. The left panel of Figure 1 shows the geometry of the collimator, while the right panel plots efficiency *vs.* system resolution for an imager having pinhole diameter $d = 0.5$ mm, an object-to-pinhole distance $b = 25$ mm, pinhole-to-detector distance $l = 210$ mm, a cone-angle $\alpha = 60°$, and detector pixel pitch $R_d = 4$ mm. These parameters are representative of imaging geometries being developed for small animal imaging.[33]

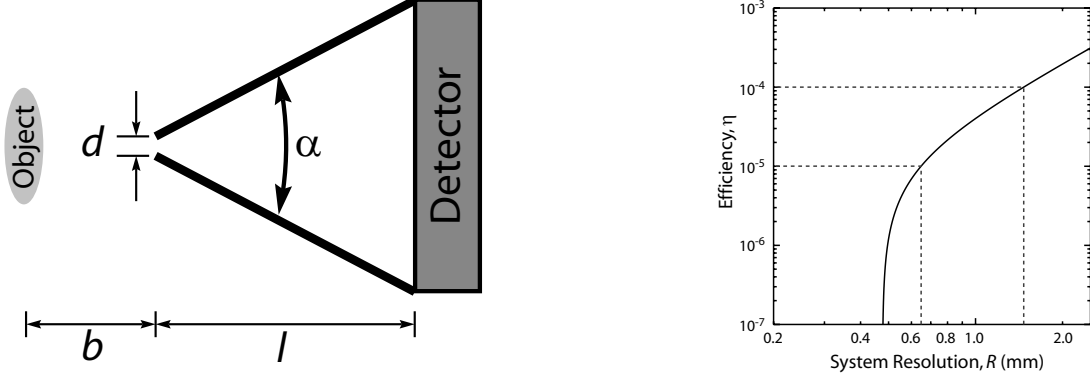**Figure 1. Left:** Geometry of a pinhole collimator, showing the dimensions of the pinhole aperture d, the field-of-view angle α, and the separation distances between the pinhole and detector l and the pinhole and object b. **Right:** Efficiency versus system resolution for a typical pinhole collimator,[33] with $l = 21$ cm, $b = 2.5$ cm, $\alpha = 60°$, $d = 0.5$ mm, and $R_d = 4$ mm. The asymptotic approach to ~ 0.5 mm resolution results from the finite pixel size of the detector. The dashed lines bound the range in resolution $R = 0.7-1.2$ mm when the efficiency is required to be $\eta = 10^{-4}-10^{-5}$ (see the text for details).

It is easy to show that the collimator resolution, R_c, is given by

$$R_c = d\left(\frac{l+b}{b}\right) \tag{1}$$

and the collimator efficiency, η is given by

$$\eta = \frac{d^2 \cos^3\theta}{16b^2}, \tag{2}$$

where l and b are the distances from the pinhole to the detector and object, respectively, d is the effective diameter of the pinhole*, and θ is the angular field of view.[34] The overall system resolution, R, depends on both R_c and the detector resolution, R_d:

$$R = \sqrt{R_c^2 + \left(\frac{R_d}{M}\right)^2}, \tag{3}$$

where M is the magnification factor that simply depends on the ratio of the two distances,

$$M \equiv \frac{l}{b}. \tag{4}$$

The right panel of Figure 1 shows how quickly the efficiency η drops as resolution R increases. The practical achievable resolution is set by the minimum efficiency requirement, driven entirely by the experimental procedures and desired image quality.

---

*Here, we have already accounted for broadening of the physical pinhole by penetration of γ-rays at the edge of the pinhole. The effective pinhole size is given by $d = \sqrt{d_0[d_0 + 2\mu^{-1}\tan(\alpha/2)]}$, where d_0 is the physical pinhole size and μ is the linear attenuation coefficient of the collimator material. For sufficiently thick and/or high-Z material and low energy photons, this effect is negligible and $d \approx d_0$.

1. The mouse must be stationary during the measurements to prevent image blurring.

2. The mouse can be under anesthesia no longer than a few hours.

3. The maximum activity that can be administered before compromising the health of the mouse is ~ 20 mCi.[33]

With these constraints, practical experience has shown that to acquire data with sufficient signal-to-noise, the efficiency must be in the range $\eta = 10^{-4}-10^{-5}$, limiting resolution to $\sim$1 mm.

1.4. A Paradigm Shift in Radionuclide Imaging

We therefore have begun developing a new high-resolution γ-ray imager for visualizing function and biomolecular processes in mice using commonly available radiopharmaceuticals labelled with either ^{125}I or technetium isotopes (^{99m}Tc, ^{95m}Tc, or ^{96}Tc). The approach is be based on recent advances in γ-ray and hard X-ray optics, which for the first time allow the development of a system that does not rely on absorptive collimation suitable for imaging γ-rays emitted by radiopharmaceuticals. (Throughout this manuscript, we interchangeably use X-ray and γ-ray to refer to photons that have energy in the range 10 keV $< E <$ 100 keV). The use of focusing optics represents a new class of instruments that are fundamentally different from existing systems–instruments that are no longer constrained by the basic conflict between efficiency and resolution that currently limits radionuclide imaging. With a low cost imaging optic, we expect to achieve spatial resolution of 100μm, an order of magnitude better than current pinhole collimator techniques.[33] The significant improvement in resolution will open new avenues of research and advance the state of the art in small animal radionuclide imaging.

2. FOCUSING X-RAY AND γ-RAY OPTICS

2.1. Basic Physics

All reflective X-ray and γ-ray focusing optics rely on the total external reflection of light, a phenomenon that results from the index of refraction n being less than unity for photons with energy above 25 eV. At these energies, the index has the form

$$n = 1 - \delta - i\beta, \tag{5}$$

where δ and β are related to the atomic scattering factors. In most instances, X-rays incident on a material are simply absorbed. But for sufficiently shallow angles, the X-rays are reflected off the surface of the material at the incident angle. The transition between reflection and absorption occurs at the critical angle, θ_c:

$$\theta_c = \sqrt{2\delta}. \tag{6}$$

The real part of the index of refraction, δ, has a strong dependence on energy, causing the critical angle to drop rapidly as photon energy increases. For example, the critical angles for iridium at 1, 10 and 100 keV are approximately 2.0°, 0.6°, and 0.1°.

2.2. Practical Configurations for Reflective X-ray Optics

Just over fifty years ago, Wolter proposed the first symmetric designs for X-ray optics.[35] Hoping to a construct a short-wavelength microscope for biological research, he realized that an efficient optic could be built using pairs[†] of conoids, a surface of revolution formed from part of a conic section (i.e., hyperbolas, parabolas, and ellipses). To meet the critical angle requirement for the total external reflection of light, the operating angles for grazing incidence systems (often referred to as Wolter optics) are typically a few degrees or less.

Limits in optical fabrication and coating techniques prevented realization of Wolter's original microscopes. His ideas remained untested until the late 1960s, when the X-ray astronomy community adopted grazing incidence designs for the first generation of X-ray telescopes.[36] A key innovation was to nest multiple pairs of mirrors inside one another, much the way Russian dolls fit inside each other, to increase efficiency by collecting light from a larger aperture. Since the launch of the first X-ray telescope aboard the *Einstein* observatory in 1978,[37] NASA,

---

[†]Even numbers of mirrors are required to (approximately) satisfy the Abbe sine rule and minimize off-axis aberration.

the European Space Agency (ESA), and the Japanese Space Agency (JSA) have built and deployed approximately ten additional X-ray astronomy satellites at a cost of several billion dollars ($US). The development of inexpensive focusing optics for radionuclide imaging will heavily leverage this significant investment and collective knowledge. Of particular importance are two recent advances that for the first time allows construction of hard X-ray ($E > 10$ keV) optics.

2.3. Key Innovations for γ-ray Optics

2.3.1. Multilayer Coatings

As discussed in Section 2.1, the critical angle drops rapidly as the photon energy increases. Even if several tens of mirrors are nested inside one another, the collection efficiency is still too low for a useable optic. One option for increasing the efficiency is to use a multilayer structure to increase the reflectivity, both in amplitude and angular acceptance. A multilayer is just a coating comprised of alternating layers of high- and low-density or high- and low-Z (atomic number) materials, e.g. molybdenum and silicon (Mo/Si) or tungsten and boron carbide (W/B_4C). Photons are reflected off the interface between the different materials according to Bragg's law:

$$m\lambda = m\frac{hc}{E} = 2d \sin\theta, \tag{7}$$

where λ is the wavelength, E is the energy, d is the bi-layer spacing, θ is the incident angle of the radiation, m is the order of the reflection, h is Planck's constant, and c is the speed of light. Recently, several researchers realized that by varying the thickness of the bi-layer throughout the coating as shown in Figure 2 (*left*), Equation 7 could be satisfied for a wide range of angles and photon wavelengths (energies).[38, 39] By carefully choosing specific combinations of the number of bi-layer pairs and grading profiles (the way d changes as a function of bi-layer number), these depth-graded multilayers can be engineered to have specific reflectivity curves.
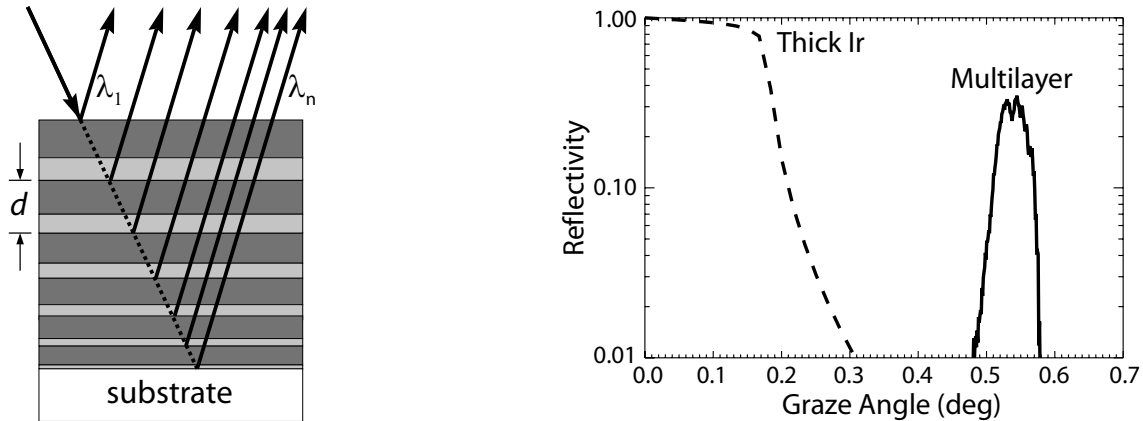

Figure 2. Left: Diagram (inspired by David Windt, http://cleuts.phys.columbia.edu/~windt.xrm/) illustrating the principles of a depth-graded multilayer. The d-spacing of each bi-layer pair decreases from top to bottom $d_1 > d_2 > \cdots > d_n$, as does the wavelength selected by each bi-layer $\lambda_1 > \lambda_2 > \cdots > \lambda_1$. **Right:** Comparison of reflectivity at $E = 27.47$ keV (the primary emission line of ^{125}I) from a thick iridium monolayer (dashed line) and a multilayer (solid line) tuned to have a response for a range of graze angles around $\theta = 0.53°$.

Figure 2 (*right*) compares the reflectivity at $E = 27.47$ keV (the photon energy of the main emission from ^{125}I) of a thick iridium coating and a multilayer coating tuned to have high response over a 0.1° angular range. The properties of a multilayer depends on several factors, including the micro-roughness of the substrates that receive the coatings and the atomic physics of the constituent materials. As a result, the reflectivity curve can only be modeled by a detailed calculation. A good empirical rule is that a multilayer can extend the range of graze angles that still have high reflectivity to three times the critical angle $\theta_{\max} \lesssim 3\theta_c$.

2.3.2. Low-cost Fabrication Techniques

The second area of innovation involves the ability to produce high-quality reflective optics at a relatively low cost, several tens of thousands of dollars ($US) for an optic with several tens of nested shells. Although this may seem expensive, when compared to the price of a pinhole, it pales next to the $700 million spent by NASA to make the four sets of mirror for the *Chandra X-ray Observatory*[40] or the tens of millions spent by ESA to make the 150 mirror shells for *XMM-Newton*.[41] To understand why reflective optics can cost so much, consider the two fabrication methods traditionally used.

The most expensive technique (used for *Chandra*) starts with a monolithic blank of high-quality ceramic glass. The mirror is literally carved from this solid, requiring extensive cycles of figuring, polishing, and metrology to achieve the desired shape and accuracy. Once the substrate is finished, a reflective coating is deposited on the interior of the optic, another expensive procedure.

Less costly than using blanks, the technique used for *XMM-Newton* is based on replication from a master. In this instance, a metal mandrel is figured and polished to the appropriate shape. Once complete, the reflective coating is deposited on the outside of the mandrel, followed by a thick nickel backing. The reflective material and its backing are then separated from the mandrel, usually by a thermal shock. Each mirror shell requires a unique mandrel, so the total cost of an optic scales with the number of mirrors, just as in the case above.

The alternative method, pioneered by Craig et al.,[42] starts with thin float glass, originally developed as a substrate for flat panel displays (e.g., laptop computer screens). This inexpensive, high-quality material has low micro-roughness of just a few angstroms, a necessary condition for achieving high reflectivity from a multilayer coating. This inherently smooth material eliminates the need for polishing, one of the most labor-intensive steps of the other techniques. The flat sheets are first thermally formed into the appropriate shape, one-fifth of a complete surface of revolution (called a quintent), either by slumping into or over an mandrel. Once the substrate has been given the appropriate shape, a multilayer is deposited on it. The final step is to assemble an optic from these separate pieces.
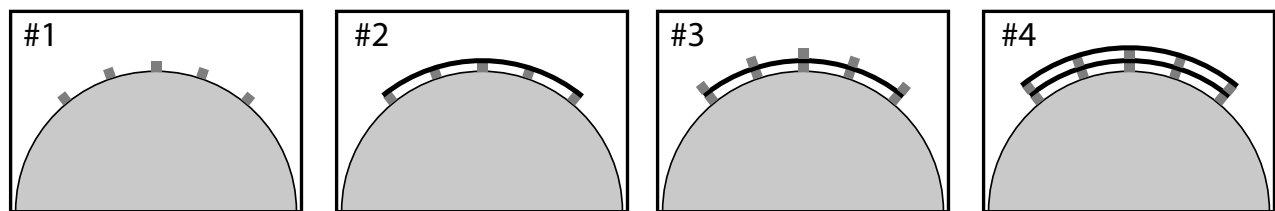

Figure 3. Schematic diagram outlining the construction process for a segmented X-ray optic. Spacers are epoxied on top of a central building mandrel and machined to the right shape (#1). A coated substrate is epoxied on top of the spacers (#2), and then another set of spacers are glued on the back surface of the fixed substrate (#3). These spacers are machined, and then the second substrate is epoxied in place (#4). The steps are repeated until all nested shells have been assembled.

The innovative solution is illustrated in Figure 3. A central building mandrel, made from titanium, aluminum or graphite is placed in a lathe. Graphite spacers are epoxied on the mandrel at regular intervals (#1). The spacers are machined to the appropriate shape and a coated substrate is glued in place (#2). A new set of spacers are glued on top of the first substrate (#3). Another coated substrate is glued in place (#4), and the process repeated until the final optic is complete. This technique has recently been used to construct a hard X-ray telescope[43] comprised of 72 nested shells that has a 1.3 arc minute half-power diameter (HPD)[‡].

[‡]The half-power diameter is a metric commonly used to describe the focusing properties of X-ray optics. It represents the diameter of a circle that encompasses half of the flux reflected by an optic. It is preferred over a Gaussian fit to the data, as the gaussian often misses the wings of the optics's response, which may contain significant flux

2.4. Near Field Optics

While there is a rich body of work detailing the design and performance of far-field grazing incidence telescopes,[36, 44–48] there are very few authors, other than Wolter,[35] that have discussed the details of near-field grazing incidence optics[§]. As such, before describing the specific requirements for an optic designed for single photon emission imaging, we quickly review the basic geometric principles of near-field γ-ray optics.

Optical designs can be classified in two broad categories: those where the diverging light is directly focused to a spot (much the way light at one foci of an ellipse is perfectly focused to the other foci), and those where the diverging light is first collimated into parallel light, and the re-focused back to a point. Except for the unique case when the magnification of the optic is set at unity, the first set of designs will have a certain degree of asymmetry (increasing as the magnification grows); we thus refer to all such designs as asymmetric. For the second set of designs, the collimation and re-focusing is done by identical combinations of conic sections; we thus refer to these designs as symmetric. Below, we consider each type of system in detail.

2.4.1. Two-Reflection Asymmetric Designs

The simplest of the asymmetric designs involves just two reflections and begins with an ellipse. On axis, the ellipse perfect focuses light leaving one foci back to the other foci. However, off-axis an ellipse has severe aberration, equal to the off-axis displacement. To correct this error, a hyperbola is placed so that it shares one foci with ellipse. Now, light leaves one elliptical foci, is reflected off the ellipse, encounters the hyperbolic surface, and is reflected off it back to the near-foci of the hyperbola. The alignment of the two conics, as well as the light path with and without the hyperbola present, is illustrated in Figure 4.
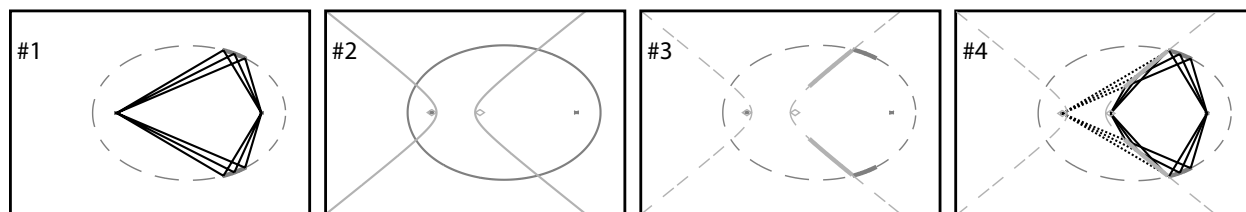

Figure 4. The basic geometry behind the two-reflection, asymmetric near-field X-ray optic. While an ellipse has perfect on-axis imaging properties (#1), it's off-axis aberration requires a secondary corrector. A hyperbola, placed so that is shares one foci of the ellipse, can largely correct the astigmatism (#2), as long as the optic consists of small portions of the surface of revolutions (#3). Now, light leaving the far foci of the ellipse is reflected off the elliptical surface, intersected and reflected by the hyperbolic surface, and properly focused to the near hyperbolic foci (#4).

2.4.2. Four-Reflection and Higher Asymmetric Designs

Building on the two-reflection design described above, additional reflective elements can easily be added. As long as the total number of reflections remains even, the Abbe sine rule can be (approximately) satisfied and an arbitrary number of hyperbolic pairs can be added. The four-reflection design would consist of three hyperbolas and one ellipse, the six-reflection design five hyperbolas and one ellipse, etc. Wolter showed that designs employing six or more reflections would perfectly correct off-axis aberration.[35]

2.4.3. Four-Reflection Symmetric Designs

Although the symmetric designs take a different approach than the asymmetric ones, they still utilize the same geometric properties of conic sections. In this instance, though, the focusing occurs in two distinct steps. First, the diverging light is made parallel, and then the collimated light is re-focused. The second part of this design performs exactly the same function as a telescope. In fact, the design of this type of near-field optic can be thought of as two far-field imaging telescopes placed end to end. Each half of the optic is based on a parabola,

which perfectly focuses parallel light to a point. A parabola suffers the same type of off-axis aberration as an ellipse, and also requires a secondary hyperbola reflection to correct the error. Thus, the fewest number of reflections for a symmetric design with good off-axis performance is four. The next design that satisfies the Abbe sine condition requires eight reflections (three hyperboloids and one paraboloid per "telescope"), the next twelve, etc.

2.4.4. Basic System Geometry

Below, we describe the basic geometry of practical near-field optical system, using a two-reflection optic with three nested mirrors (shown in Figure 5 to guide the discussion of the system parameters. The focal length f is the separation distance between the animal and the detector and is simply the sum of the distance between the middle of the optic and mouse f_1 and the middle of the optic and the detector f_2:

$$f = f_1 + f_2. \tag{8}$$

The magnification of the optic M is the ratio of the two sub-focal lengths

$$M = \frac{f_2}{f_1}, \tag{9}$$

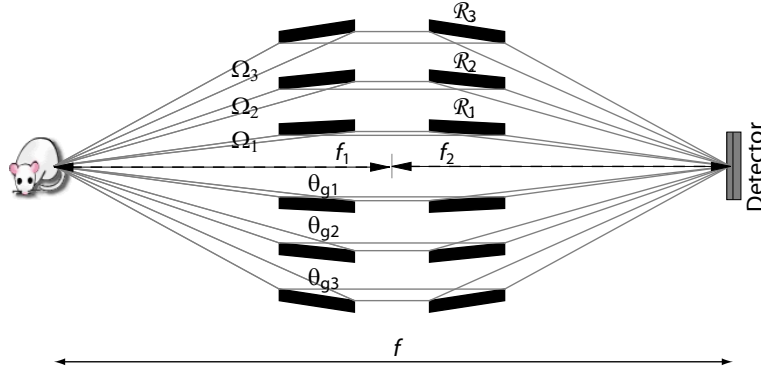and is always unity for symmetric designs.

Figure 5. Exploded view of a two-reflection asymmetric optic with three sets of nested mirror or shells. While the case illustrated has $f_1 = f_2$, resulting in unity magnification $M = f_2/f_1 = 1$, f_1 must only equal f_2 for symmetric optical designs. Refer to the text for more discussion on the labelled parameters.

Each of the nested mirrors (or shells) is essentially its own individual optic, with the total system characteristics (e.g., efficiency) determined by summing the properties of each shell. Starting with the smallest radius inner shell and moving outwards, the solid angle subtended by each shell Ω_i and the graze angles reflected off each substrate $\theta_{\mathrm{g}i}$ increase:

$$\theta_{\mathrm{g}N} > \cdots > \theta_{\mathrm{g}3} > \theta_{\mathrm{g}2} > \theta_{\mathrm{g}1} \tag{10}$$

and

$$\Omega_N > \cdots > \Omega_3 > \Omega_2 > \Omega_1, \tag{11}$$

where the optic consists of N shells, and the smallest subscript refers to the inner-most shell. The multilayers deposited may also change with shell number. In one extreme, all substrates will have the same coating, while at the other extreme, each substrate will have its own specific coating. Regardless of the precise multilayer recipe, the different graze angles will result in a different average reflectance $\Re_i$. Usually, the inner-most shells have the highest reflectivity, and the general trend that emerges follows

$$\Re_N \lesssim \cdots \lesssim \Re_3 \lesssim \Re_2 \lesssim \Re_1. \tag{12}$$

The total efficiency η is the sum of individual shell efficiencies η_i

$$\eta = \sum_1^N \eta_i = \sum_1^N \Omega_i \Re_i^J, \tag{13}$$

where J is the number of reflections required to focus the light ($J = 2$ for design shown in Figure 5).

3. SARIS: SMALL ANIMAL RADIONUCLIDE IMAGING SYSTEM

For the last two years, our collaboration has worked to develop γ-ray optics for single photon emission imaging. To date, our collaboration has three major successes:

1. We have written an extensive suite of ray-tracing routines, analysis tool and design engines for simulating and evaluating all types of near-field X-ray and γ-ray optics.

2. We have engineered and constructed a T-based lathe with micron precision to construct optics from segmented substrates, adopting and modifying the scheme of Craig et al..[42]

3. We have fabricated and tested two prototype optics, a four-reflection symmetric design and a two-reflection asymmetric design.

3.1. Simulation Capabilities

3.1.1. Basic Design Considerations

There are four parameters that will influence the final prescription of a focusing optic built for radionuclide imaging: the photon energy E emitted by the radiopharmaceutical, the field of view (FOV)needed, the minimum acceptable efficiency η and the desired resolution R. Table 1 lists the parameters and their requirements, and how they influence the two related, but distinct components of the optical system: the optical design that determines the physical size and shape of the mirrors and the multilayer recipes that determines the reflectivity properties of the coatings deposited on the substrate surfaces. The goal of imaging a mouse drives the values of all the requirements. For example, the size of a typical mouse determines the $1-3$ cm FOV.

Table 1. Factors and Requirements That Drive The Prescription of a Radionuclide Imaging Optic

		Strongly Influences	
Parameter	Requirement	Optical Design	Multilayer Recipe
Photon Energy (E)	$\gtrsim 15$ keV	no	yes
Field-of-view (FOV)	$1-3$ cm diameter	yes	no
Resolution (R)	$\leqq 100~\mu$m	yes	no
Efficiency (η)	$\geqq 10^{-5}$	no	yes

3.1.2. Optical Design

Here, the optical design refers to the physical size of the optic (e.g., length of the individual mirrors), configuration (e.g., number of shells N and the focal length f) and the design type (e.g., two-reflection asymmetric). By far the most important parameter is f, which influence both the FOV and resolution. This is easiest to understand by first considering the angular properties of an optic. A Wolter optic has an angular view $\Delta\Theta$ exactly analogous to the viewing angle α of a pinhole collimator (refer to Figure 1). The physical FOV on the γ-ray optic, then, will simply be

$$\text{FOV} = 2f \times \tan\Delta\Theta/2 \approx f \times \Delta\Theta, \tag{14}$$

where $\Delta\Theta$ will depend on several factors, including the length of the mirrors, the graze angle, and the packing fraction of the nested shells. The spatial resolution follows a similar relationship, although now the relevant

angular characteristic is the quality of the substrates. Although several factors determine how well a X-ray optic will focus light, a single value that represents the quality of the mirror substrate can successfully be used to describe its overall performance, when measured by a standard metric, like the half-power diameter (HPD) or the gaussian full width at half maximum (FWHM). Thus, the spatial resolution of our γ-ray optic equals

$$R = 2f \times \tan\theta_Q \approx f \times \theta_Q, \tag{15}$$

where θ_Q represent the angular quality of the thermally formed substrate.

3.1.3. Multilayer Recipe

The most important factor in determining the prescription for the multilayer is the photon energy emitted by the radionuclide. Certain energies are best reflected by particular material combinations. For example, molybdenum is the material of choice when focusing the low-energy lines (between 17.4 keV and 18.4 keV) emitted by ^{95m}Tc, ^{96}Tc, and ^{99m}Tc because the K absorption of Mo occurs at 20 keV. By operating at energies right below the K edge, the reflectivity of multilayers made from Mo remain high ($\Re \gtrsim 20\%$) out to graze angles of almost 1.0°. At the 27.5 keV, which is right above its K edge, Mo is a poor choice for a multilayer. Instead, higher atomic number materials like tungsten result in coatings with higher reflectivity.

Once the optimal materials have been identified, there are several other important considerations to make, all of which have complex relations to one another. One such factor is how much the multilayer should be depth-graded. As coatings are made with larger spans in the bilayer thickness, they can reflect X-rays over a larger range of graze angles. But as the angular acceptance increases (this has some influence on $\Delta\Theta$ in Equation 14), the overall reflectivity will drop.

3.1.4. Detailed Simulations and Optimizations

Meeting all the specifications detailed in Table 1, while accurately modeling all the factors that influence the multilayer recipe and optical design, requires searching a large, multi-variable parameter space. We have developed ray-tracing codes, based on Monte Carlo techniques, that account for all possible geometries, as well as the finite reflectivity of the multilayer coatings. We have used our current suite of Monte-Carlo-based simulations to design and model several complete systems,[51] including a four-reflection symmetric design for ^{125}I imaging that consists of 102 nested shells and has $R = 145$ μm and $\eta = 2 \times 10^{-5}$.

3.2. High-Precision Lathe for X-ray Optics

It is beyond the scope of this paper to discuss in detail the design, construction and operation of the T-based lathe fabricated specifically for the purpose of making γ-ray optics for biomedical research. However, it is important to briefly discuss the highlights of this machine, shown in Figure 6. All the components sit on a granite table, providing good thermal stability and vibration control. The granite table and control computers are kept in a temperature-controlled room to minimize the influence of thermal variations. The core of the machine is two sets of interferometrically controlled friction drives that control the position of a cutting tool. This cutting tool allows precision machining of the spacers used to locate the substrates (as described in Section 2.3.2). The optic remains at a fixed position, spinning in a pair of air bearing spindles, as the cutting tool moves across the face of the optic, grinding the spacers into their appropriate shape. Metrology of finished parts indicate that the current configuration of the machine has 1 μm accuracy and precision, well within the specifications needed to make high-quality optics.

3.3. Initial Results from a Prototype 27.5 keV γ-ray Optic

3.3.1. Experimental Set-up

To verify that X-ray optics can be used for small animal imaging, we have constructed two prototype optics: a four-reflection symmetric prototype and a two-reflection asymmetric optic with unity magnification. In both instances, the optic contains only a small subset of the full complement of $50-100$ shells needed to obtain useful efficiencies. Below, we present result from the asymmetric prototype.

Budgetary constraints prevented us from fabricating substrates specifically for biomedical imaging. Instead, we used thermally-formed substrates produced originally for astrophysical telescopes. The radius of glass ($r =$
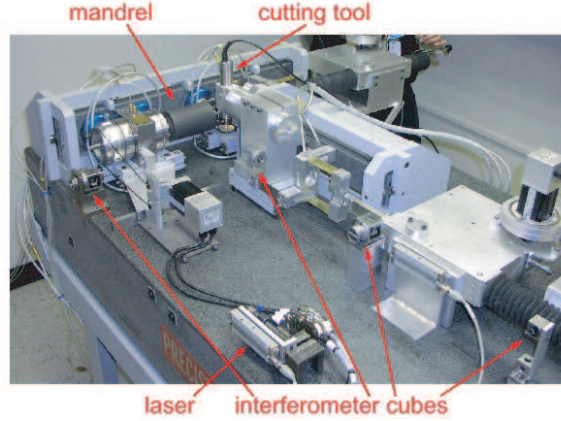
Figure 6. Photograph of high-accuracy T-based lathe designed and constructed for making segmented X-ray and γ-ray optics. Housed in a temperature controlled room, the micron precision results from interferometrically controlled friction drives and the use of air bearing spindles.

$39 - 44$ mm) drove the optical design, while the multilayer coatings, comprised of W/Si 220 bi-layers, were tuned to focus 27.5 keV photons, corresponding to the brightest emission line from ^{125}I. The reflectivity from the coating is shown in the right panel of Figure 3. Table 2 lists the basic properties of the prototype. The long focal

Table 2. Characteristics of the 27.5 keV Prototype Optic

Property	Value	Property	Value
Design Type	2-reflection asymmetric	Number of Shells, N	2
Photon Energy, E	27.5 keV	Efficiency, η	5×10^{-7}
Focal Length, f	4.3 m	Substrate Quality	$50 - 75''$
Magnification, M	1.0	Expected Resolution, R	$1.0 - 1.6$ mm HPD
On-axis Graze Angles, θ_g	$\sim 0.5°$	Measured Resolution, R	1.5 mm HPD
Multilayer Coating	220 W/Si bilayer pairs		

length (set by the radius of the glass), the modest quality of the substrates, and small number of shells will result in an optic that has low efficiency and ~ 1 mm resolution far from the ultimate goals of the project. However, the intent when building the prototypes was only to demonstrate the overall feasibility of using focusing γ-rays optics for near-field imaging. Given sufficient resources to make substrates, the focal length will decrease, the mirror quality will improve, and the resolution and efficiency will quickly approach the target goals of $R = 100 \ \mu$ and $\eta > 10^{-5}$.

Figure 7 shows the experimental setup used to evaluate the optic. Although designed to focus emission from ^{125}I, the low efficiency of the prototype and difficulty in obtaining a bright, point-like iodine source required use of different a source. The high intensity and small spot ($\sim 100 \ \mu$m) of an X-ray tube make it an ideal substitute. In this case, the tungsten anode tube was run at 0.5 mA current and 50 kV to ensure that the bremsstrahlung radiation peaked at 27 keV, corresponding to the energy range of the multilayer coatings. Because the spot of the X-ray tube is small compared to the expected resolution, it can essentially be considered a point-source. Although the ideal detector would be a single photon counting device with sub-100 μm pixels, e.g. a pixelated high-purity Ge array,[52] scintillator detectors are a good alternative. Here, we have used a phosphor-CCD system designed for microCT of small animals using a Gd_2O_2S screen coupled via taper to a 1024×1024 CCD. The pixel size of the detector at the phosphor is 70 μm, resulting an imaging area 7 cm on side.
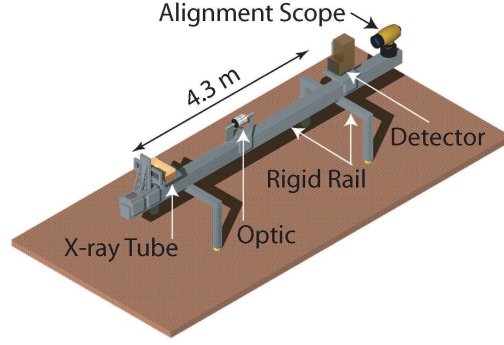
Figure 7. Engineering drawing showing the experimental set-up used to test the two-shell, two-reflection optic tuned for ^{125}I imaging. The X-ray tube, optic and detector are positioned with the alignment scope on a rigid rail that is vibrationally isolated from the laboratory. The X-ray tube is rastered across the field of view and driven in and out of focus with translation stages.

3.3.2. Measurements

The first step is to find the best-focus of the optic. The X-ray tube, optic and detector were placed at the appropriate distances specified by the optical design. Once co-aligned, the optic was held fixed and the detector and X-ray tube were moved. Alignment begins by moving the X-ray tube across the face of the optic. The CCD images were analyzed to find the smallest spot. This defines the optical axis of the system. Next, the X-ray tube was driven along the optical axis, again looking for the smallest spot in the CCD data. Once this was accomplished, the detector was moved in a similar fashion to find its best focus.

Once the X-ray tube and detector were aligned, we systematically rastered the X-ray tube across the field-of-view (FOV) of the optic. Figure 8 (*left*) shows a composite image formed from adding CCD frames when the X-ray tube was on-axis (X = 0, Y = 0) and when it was ±4,±6, ±8, and ±10 off-axis in the X or Y direction. For comparison, Figure 8 (*right*) shows the a similar composite image formed by ray-trace simulations of the optic. There is excellent agreement between the experimental and simulated data. Of particular interest is that the spots in the ±X direction are weaker than those in the ±Y direction. This results from a construction error in the optic. The epoxy bond failed for one of the substrates and, since the mirror is incorrectly located, the light that reflects off that surface is improperly focused. To prevent this quintent from degrading the performance, we blocked off one-fifth of the optic with a thick piece of lead. When we accounted for this in the ray-tracing simulations, the flux in the X direction is diminished, just like in the actual data.

We carefully analyzed the on-axis data and calculate a half-power diameter of 1.5 mm. A Gaussian fit to the data reveals a narrow core, with a full-width half-maximum (FWHM) value of 1.0 mm. This corresponds to an angular spot size of 72 arc-seconds (HPD) with a narrow core of 48 arc-seconds (FWHM), consistent with the quality of the substrates (see Table 2). The excellent agreement between the measured and simulated point spread functions, as well as the agreement between the measured on-axis spot and predicted performance, are very encouraging. It validates the overall approach of using γ-ray optics for near-field imaging, and indicates that once small radius substrates are fabricated, a practical small animal imaging system with high resolution and efficiency can be constructed.

4. CONCLUSION

Current techniques for single photon emission (radionuclide) imaging studies rely on absorptive collimation, an approach that has a strict relationship between efficiency and resolution. Efficiency requirements effectively constrain these methods to a spatial resolution no better than ∼1 mm, limiting investigation of several important areas of biomedical research. Focusing X-ray and γ-ray optics, using recent advances pioneered by the high-energy astrophysics community, provide a way to break the paradigm that ties resolution to efficiency and offer a path to imaging small animals with 100 μm resolution.
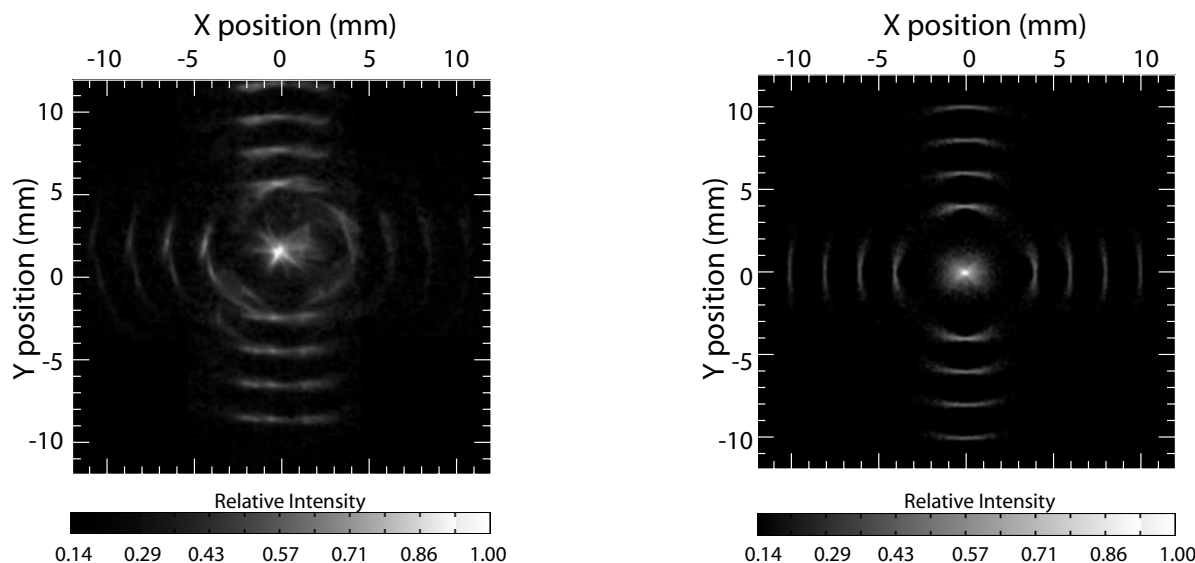
Figure 8. Measured and simulated point spread function for the asymmetric prototype optic. **Left:** Composite images formed by summing individual exposures when the X-ray tube was located on-axis (X = 0, Y = 0) and at (X = $\pm 4, \pm 6, \pm 8, \pm 10$ mm, Y = 0) and (X = 0, Y = $\pm 4, \pm 6, \pm 8, \pm 10$ mm). **Right:** Similar image formed from simulated data.

Our collaboration has spent two years developing γ-ray optics specifically for this purpose. Through careful Monte Carlo simulation of optical designs and multilayer recipes, we have demonstrated that practical optics can be built that have efficiencies of at least 10^{-5} (comparable to pinhole systems that provide $\sim$0.75 mm resolution) and spatial resolution at least an order of magnitude better than the state-of-the-art pinhole collimator systems. Preliminary results from our first prototype optics verify the feasibility of this approach and our optical designs.

ACKNOWLEDGMENTS

REFERENCES

1. A. Bernstein and M. Breitman, "Genetic ablation in transgenic mice," *Molecular Biol Med* **6**, pp. 523–530, 1989.
2. X. Gao, A. Kemper, and B. Popko, "Advanced transgenic and gene-targeting approaches," *Neurochem Res* **24**, pp. 1181–1188, 1999.
3. J. N. Crawley, "Behavioral phenotyping of transgenic and knockout mice: experimental design and evaluation of general health, sensory functions, motor abilities, and specific behavioral tests," *Brain Res* **835**, pp. 18–26, 1999.
4. R. Brusa, "Genetically modified mice in neuropharmacology," *Pharamacol Res* **39**, pp. 405–419, 1999.
5. U. Rudolph and H. Mohler, "Genetically modified animals in pharmacological research: future trends," *Europ J Pharmacol* **375**, pp. 327–337, 1999.
6. G. E. Homanics, J. J. Quinlan, R. M. Mihalek, and L. L. Firestone, "Alcohol and anesthetic mechanisms in genetically engineered mice," *Front Biosci* **8**, pp. D548–D558, 1998.

7. J. L. Viney, "Transgenic and gene knockout mice in cancer research," *Cancer Metast Rev* **14**, pp. 77–90, 1995.

8. J. A. Gossen, W. J. de Leeuw, and J. Vijg, "LacZ transgenic mouse models: their application in genetic toxicology," *Mutation Res* **307**, pp. 451–459, 1994.

9. D. Hanahan, "Transgenic mice as probes into complex systems," *Science* **246**, pp. 1265–1275, 1989.

10. P. Carter and A. M. Merchant, "Engineering antibodies for imaging and therapy," *Biotechnology* **8**, pp. 449–454, 1997.

11. K. D. Becker, K. R. Gottshall, and K. R. Chien, "Strategies for studying cardiovascular phenotypes in genetically manipulated mice," *Hypertension* **27**, pp. 495–501, 1996.

12. J. F. James, T. E. Hewett, and J. Robbins, "Cardiac physiology in transgenic mice,"

13. S. S. Gleason, H. Sari-Sarraf, M. J. Paulus, and D. K. Johnson, "Reconstruction of multi-energy x-ray computed tomography of laboratory mice," *IEEE Trans Nucl Sci* **46**, pp. 1081–1086, 1999.

14. M. J. Paulus, H. Sari-Sarraf, S. S. Bleason, and M. Bobrek, "A new x-ray computed tomography system for laboratory mouse imaging," *IEEE Trans Nucl Sci* **46**, pp. 558–564, 1999.

15. M. Ding, A. Odgaard, and I. Hvid, "Accuracy of cancellous bone volume fraction measured by micro-CT scanning," *J Biomech* **32**, pp. 323–326, 1999.

16. R. E. L, M. E. Bolander, L. A. Fitzpatrick, and R. T. Turner, "Micro-CT imaging of structure-to-function relationship of bone microstructure and associated vascular involvement," *Technol Health Care* **6**, pp. 403–412, 1998.

17. R. F. Kooy, E. Reyniers, M. Verhoye, J. Sijbers, C. E. Bakker, B. A. Oostra, P. J. Willems, and A. Van Der Linden, "Neuroanatomy of the fragile knockout mouse brain studies using in vivo high resolution magnetic resonance imaging," *Europ J Human Genetics* **7**, pp. 526–532, 1999.

18. R. E. Jacobs, E. T. Ahrens, T. J. Meade, and S. E. Fraser, "Looking deeper into vertebrate development," *Trends Cell Biol* **9**, pp. 73–76, 1999.

19. S. Siegel, J. J. Vacquero, A. L, and J. Seidel, "Initial results from a PET/planar small animal imaging system," *IEEE Trans Nucl Sci* **46**, pp. 571–575, 1998.

20. S. R. Meikle, S. Eberl, R. R. Fulton, and M. Kassiou, "The influence of tomograph sensitivity on parameter estimation in small animal imaging studies," *1998 IEEE Nuclear Science Symposium and Medical Imaging Conference* **3**, pp. 1898–1903, 1998.

21. J. A. Correia, C. A. Burnham, D. Kaufman, and A. J. Fischman, "Development of a small animal PET imaging device with resolution apporaching 1 mm," *IEEE Trans Nucl Sci* **46**, pp. 631–635, 1999.

22. R. S. Miyaoka and T. K. Lewellen, "Design analysis of a high resolution detector block for a low cost small animal positron imaging system," *1994 IEEE Nuclear Science Symposium and Medical Imaging Conference* **3**, pp. 1370–1374, 1994.

23. S. R. Cherry, Y. Shao, R. W. Silverman, and K. Meadors, "MicroPET: a high resolution PET scanner for imaging small animals," *IEEE Trans Nucl Sci* **44**, pp. 1161–1166, 1997.

24. J. S. Fowler, N. D. Volkow, G. J. Wang, Y. S. Ding, and S. L. Dewey, "PET and drug research and development," *J Nucl Med* **40**, pp. 1154–1163, 1999.

25. L. Tian, "Two quantitative methods for imaging samples in molecular biology," *Clin Chem Lab Med* **36**, pp. 589–591, 1998.

26. N. Kusaka, T. Takeda, A. Hoshino, T. Horoiwa, T. Yuasa, T. Akatsuka, and Y. Itai, "Development of multispectral autoradiography with solid state detector," *Medinfo* **9**, pp. 1036–1040, 1998.

27. P. Laniece, Y. Charon, A. Cardona, L. Pinot, S. Maitrejean, R. Mastrippolito, B. Sandkamp, and L. Valentin, "A new high resolution radioimager for the quantitative analysis of radiolabelled molecules in tissue section," *J Neurosci Meth* **86**, pp. 1–5, 1998.

28. A. G. Weisenberger, E. L. Bradley, S. Majewski, and M. S. Saha, "Development of a novel radiation imaging detector system for in vivo gene imaging in small animal studies," *1996 IEEE Nuclear Science Symposium* **2**, pp. 1201–1205, 1996.

29. A. G. Weisenberger, E. L. Bradley, S. Majewski, and M. S. Saha, "CsI(Na) based radiation detector for high resolutino imaging studies using iodine 125 in small-animal research," *Proc SPIE* **3115**, pp. 254–262, 1997.

30. A. G. Weisenberger, E. L. Bradley, S. Majewski, and M. S. Saha, "Development of a novel radiation imaging detector system for in vivo gene mapping in small animals," *IEEE Trans Nucl Sci* **45**, pp. 1743–1749, 1998.

31. M. W. Dae, J. W. O'Connell, E. H. Botvinick, and M. C. Chin, "Acute and chronic effects of transient myocardial ischemia on sympathetic nerve activity, density, and norepinephrine content," *Cardiovasc Res* **30**, pp. 270–280, 1995.

32. N. M. Caplice and B. J. Gersh, "Stem cells to reapir the heart: a clinical perspective," *Circ Res* **92**, pp. 6–8, 2003.

33. M. C. Wu, B. H. Hasegawa, and M. W. Dae, "Peformance evaluation of a pinhole SPECT system for myocardial perfusion imaging of mice," *Med Phys* **9**, pp. 2830–2839, 2002.

34. J. A. Sorenson and M. E. Phelps, *Physics in Nuclear Medicine*, W. B. Saunders Company, Philadelphia, 1987.

35. H. Wolter, "Spiegelsysteme streifenden Einfalls als abbildende Optiken für Röntgenstrahlen," *Ann Physik* **10**, pp. 94–114, 1952.

36. J. D. Mangus and J. H. Underwood, "Optical design of a glancing incidence x-ray telescope," *Applied Optics* **8**, pp. 95–102, 1969.

37. R. Giacconi *et al.*, "The Einstein (HEAO 2) x-ray observatory," *Astrophys J* **230**, pp. 540–550, 1979.

38. A. Walker, O. R. H. Lindblom, J F, R. B. Hoover, and T. W. J. Barbee, "Astronomical observations with normal incidence multilayer optics: recent results and future prospects," *Physica Scripta* **41**, pp. 1053–1062, 1992.

39. F. E. Christensen, A. Hornstrup, N. J. Westergaard, H. W. Schnopper, J. Wood, and K. Parker, "A graded d-spacing multilayer telescope for high energy x-ray astronomy," *Proc SPIE* **1546**, pp. 160–167, 1992.

40. M. C. Weisskopf, H. D. Tananbaum, and L. P. Van Sprefybroeck, "Chandra x-ray observatory (CXO): overview," *Proce SPIE* **4012**, pp. 2–16, 2000.

41. F. D. Jansen *et al.*, "XMM-Newton observatory. I. the spacecraft and operations," *Astron Astrophys* **365**, pp. L1–L6, 2001.

42. W. W. Craig, C. J. Hailey, M. Jimenez-Garate, D. L. Windt, F. A. Harrison, P. H. Mao, F. E. Christensen, and A. M. Hussain, "Development of thermally formed glass optics for astronomical hard x-ray telescopes," *Optics Exp* **7**, pp. 178–185, 2000.

43. J. E. Koglin, J. Chonko, F. E. Christensen, W. W. Craig, T. R. Decker, C. J. Hailey, F. A. Harrison, C. P. Jensen, M. Stern, D. L. Windt, and H. Yu, "Production and development of precision hard x-ray multilayer optics," *Proc SPIE* **5168**, 2003.

44. L. P. VanSpeybroeck and R. C. Chase, "Design parameters of paraboloid-hyperboloid telescopes for x-ray astronomy," *Applied Optics* **11**, pp. 440–445, 1972.

45. W. Werner, "Imaging properties of Wolter I type x-ray telescopes," *Applied Optics* **16**, pp. 764–773, 1977.

46. B. Aschenbach, "X-ray telescopes," *Rep Prog Phys* **48**, pp. 579–629, 1985.

47. C. J. Burrows, R. Burg, and R. Giacconi, "Optimal grazing incidence optics and its application to wide-field x-ray imaging," *Astrophys J* **392**, pp. 760–765, 1992.

48. P. Conconi and S. Campana, "Optimization of grazing incidence mirrors and its application to surveying X-ray telescopes," *Astron Astrophys* **372**, pp. 1088–1094, 2001.

49. P. Troussel, P. Munsch, and J.-J. Ferme, "Microfocusing between 1 and 5 keV with Wolter type optics," *Proc SPIE* **3773**, pp. 60–69, 1999.

50. H. Takano *et al.*, "X-ray scattering microscope with a Wolter mirror," *Rev of Scien Instr* **73**, pp. 2629–2633, 2002.

51. M. J. Pivovaroff, W. Craig, K. Ziock, W. Barber, K. Iwata, and B. H. Hasegawa, "Design of gamma-ray optics for small animal imaging," *J Nucl Med* **43**(5sup), pp. 231–232, 2002.

52. H. B. Barber, F. L. Augustine, H. H. Barrett, E. L. Dereniak, J. D. Eskin, D. G. Marks, K. J. Matherson, J. E. Venzon, J. M. Woolfenden, and E. T. Young, "High-resolution imaging using a 48×48 Ge array with multiplexer readout," *1996 IEEE Nucl Sci Symp Med Imaging Conf* **1**, pp. 113–117, 1996.